Solving Einstein's Equation Numerically on Manifolds with Non-Orientable Spatial Slices

Fan Zhang [a,b] and Lee Lindblom [c]
[a] *Institute for Frontiers in Astronomy and Astrophysics, Beijing Normal University, Beijing 102206, China*
[b] *Gravitational Wave and Cosmology Laboratory, School of Physics and Astronomy, Beijing Normal University, Beijing 100875, China and*
[c] *Center for Dark Cosmology and Gravitation, Department of Physics, University of California at San Diego, La Jolla, CA 92093, USA*
(Dated: December 8, 2025)

This paper presents solutions to Einstein's equation—and the numerical methods used to construct them—that describe simple cosmological models on manifolds with compact non-orientable spatial slices. These solutions have been constructed on a selection of manifolds having positive, negative, and vanishing spatial scalar curvatures. One example is shown to be indistinguishable locally from a homogeneous Friedman cosmological model, others are constructed with significant inhomogeneities. Together these examples are used to explore the strengths and the limitations of the numerical methods used in this study, and to test the code used to implement them.

I. INTRODUCTION

Einstein's equation determines the geometry of spacetime given initial data for the matter fields (and any gravitational waves) that may be present on a spacelike surface. This equation does not, however, determine the topology of that initial spatial slice. That topology must be specified independently to insure the solutions faithfully model a particular physical problem. Solutions to Einstein's equation have been studied on manifolds with a small number of simple topologies, e.g., with initial surfaces having S^3, T^3, or $S^2 \times S^1$ topologies, etc. But little is known about solutions on manifolds from most of the infinite collection of possible topologies. Current observations do not determine or even constrain the possible topology of our universe. Therefore it seems reasonable to explore the properties of solutions on manifolds having a wide variety of possible topologies. To that end robust numerical methods have been developed—and implemented in an efficient computer code—that facilitate the study of solutions to Einstein's equations on manifolds with arbitrary spatial topologies [1–4]. This study extends that work by constructing and analyzing solutions to Einstein's equations on manifolds with non-orientable spatial slices.

Space-times with non-orientable topologies are often dismissed as nonphysical because analysis shows that only certain types of global spinor structures are allowed on such manifolds [5–7]. These arguments probably rule out the possibility that the observable part of our universe is time or space non-orientable. However, they do not rule out the possibility that spatial slices could become non-orientable when extended beyond our cosmic horizon.

This study has three primary goals. The first is to demonstrate that it is possible to find solutions to Einstein's equation on manifolds with non-orientable topologies. The second is to explore whether homogeneous solutions on non-orientable manifolds can be distinguished in some way locally from the standard homogeneous Friedman cosmological models. The third goal is to explore and evaluate the strengths and limitations of the numerical methods that have been developed to solve Einstein's equation on manifolds with arbitrary spatial topologies. For example, the code developed to solve the covariant representation of the Einstein evolution equations (needed for non-trivial topologies) has only been tested previously by evolving solutions with small amplitude gravitational wave perturbations on a manifold with S^3 spatial topology [2]. In this study the code is tested more robustly by evolving the fully nonlinear equations long enough to expand the spatial volumes of the solutions by a factor of ten.

The remainder of this paper is organized as follows. The simple non-orientable manifolds used in this study are described in Sec. II. This section describes the multicube representations of these manifolds, including the construction of the reference metrics needed to define their differentiable structures. This section also demonstrates that the manifolds included in this study satisfy the topological conditions needed to admit global Dirac and Majorana (but not Weyl) spinor structures.

Section III describes the methods used to construct simple initial data that satisfy the Einstein constraint equations on these manifolds. These initial data were found by solving a version of the Einstein constraints for a spacetime devoid of matter except for a cosmological constant. The value of this constant is chosen in each example to produce a geometry with a homogeneous spatial Ricci scalar curvature. The quality of these numerical solutions are evaluated, and the convergence of the numerical methods used to solve the elliptic constraint equations is illustrated.

Section IV describes and analyzes the numerical evolution of these initial data which produce simple non-orientable cosmological models. One of these models is shown to be indistinguishable locally from one of the standard homogeneous Friedman cosmological models.

The other examples have significant inhomogeneities that grow rapidly from inhomogeneities present in the initial data for these cases. Together these examples provide an opportunity to evaluate the strengths and limitations of the numerical methods and their implementation in the computer code used to solve the hyperbolic Einstein evolution equations. The covariant symmetric hyperbolic representation of the Einstein evolution equations used in this study is described briefly in Appendix A. Section V presents a summary and discussion of the results of this study, including ideas that could be pursued to address some open questions.

II. SIMPLE NON-ORIENTABLE MANIFOLDS

This section describes the simple non-orientable manifolds on which solutions to Einstein's equation have been constructed for this study. Each of these four-dimensional manifolds has the topology of a globally hyperbolic spacetime, i.e. its topology has the form $\mathbb{R} \times \Sigma$, where Σ is a compact non-orientable three-dimensional manifold. This study uses multi-cube representations of the three-manifolds, Σ, to facilitate the numerical analysis. These multi-cube representations (introduced in Ref.[1]) are collections of non-overlapping cubic regions which serve as coordinate patches that cover the manifold.

Figure 1 illustrates the multi-cube structures for three of the manifolds used in this study: $P^2 \times S^1$, $P^2 \# P^2 \times S^1$ and $P^2 \# T^2 \times S^1$. Each of these manifolds is the Cartesian product of a non-orientable compact two-manifold with the circle, S^1. P^2 represents the two-dimensional real projective plane and T^2 the two-torus, while $\times$ indicates a Cartesian product and $\#$ a direct sum. These manifolds are represented as a collection of non-overlapping cubic regions whose faces are identified in the prescribed way. Figure 1 illustrates the $+z$ faces of the cubic regions representing these manifolds, including the way the x and y faces are identified. The $+z$ and $-z$ face of each of these cubic region is identified to implement the Cartesian product with S^1.

Figure 2 illustrates the other compact non-orientable three-manifold used in this study: $S^2 \tilde{\times} S^1$, where S^2 and S^1 are the two-sphere and the circle respectively, while $\tilde{\times}$ represents a twisted Cartesian product (described below). The locations of the blocks in this structure are the same as those used in the multi-cube structure of $S^2 \times S^1$ introduced in Ref. [1]. In $S^2 \times S^1$ the $+z$ face of each block is identified with the $-z$ face of that block. In $S^2 \tilde{\times} S^1$ the $+z$ face of each block is identified with the $-z$ face of the block containing its polar opposite points in S^2. In this way the $+z$ face of region $\mathcal{B}_1$ is identified with the $-z$ face of region $\mathcal{B}_3$, the $+z$ face of region $\mathcal{B}_2$ is identified with the $-z$ face of region $\mathcal{B}_4$, the $+z$ face of region $\mathcal{B}_5$ is identified with the $-z$ face of region $\mathcal{B}_6$, etc.

The Euler characteristic of the Cartesian product of two manifolds is the product of the Euler characteristics

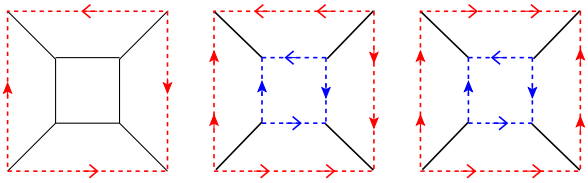

FIG. 1: This figure illustrates the $+z$ faces of the multi-cube blocks representing three of the compact non-orientable three-manifolds used in this study: (from left to right) $P^2 \times S^1$, $P^2 \# P^2 \times S^1$, and $P^2 \# T^2 \times S^1$. The solid (black) lines represent the x and y boundary faces between adjacent blocks, while the dashed lines represent faces that are identified with the faces having similar arrows, in the directions indicated by those arrows. The $+z$ face of each block is identified with the $-z$ face of that block.

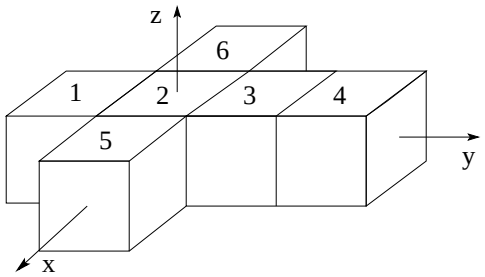

FIG. 2: This figure illustrates the multi-cube structure used in this study for the compact non-orientable three-manifold $S^2 \tilde{\times} S^1$.

of the individual manifolds. Since the Euler characteristic of S^1 is zero, the Euler characteristics of the manifolds $P^2 \times S^1$, $P^2 \# P^2 \times S^1$, and $P^2 \# T^2 \times S^1$ are also zero. The multi-cube structure of the manifold $S^2 \tilde{\times} S^1$ shown in Fig. 2 has the same number of vertices, edges, faces, and volumes as the multi-cube structure of $S^2 \times S^1$, therefore its Euler characteristic is also zero. Dirac and Majorana spinor structures do exist on a non-orientable manifold if the Euler characteristic of that manifold is an even integer [7]. It follows that all the non-orientable manifolds included in this study do admit global Dirac and Majorana spinor structures. These manifolds do not admit global Weyl spinor structures [5, 6], however, Weyl spinor structures do exist on any orientable submanifold. These orientable submanolds can extend in some cases through the cosmic horizon. Therefore it seems unlikely that non-orietability on a global scale can be ruled out by observations at this time.

The Cartesian coordinates within each cubic region in a multi-cube representation of a manifold serve as local coordinate patches on which scalar, vector and tensor fields can be represented on this manifold. The maps used to identify the faces of neighboring cubes in these structures are used to determine when scalar fields are continuous across those faces. Since the cubic regions do not overlap, however, in general these boundary maps do not determine when vector and tensor fields are contin-

uous across those interfaces. More geometric structure must be provided to determine the continuity of vector and tensor fields across the interface boundaries between cubic regions.

The additional structure needed to determine the continuity and differentiability of vector and tensor fields across the interface boundaries in a multi-cube representation can be provided by a "reference metric" that is suitably smooth (typically at least $\mathcal{C}^1$) [1]. These reference metrics can be constructed numerically using the method described in detail in Ref. [3] for two-dimensional multi-cube structures and in Ref. [8] for three-dimensional structures. This method constructs a sequence of increasingly smooth metrics that ensure the final reference metric, $\tilde{g}_{ij}$, is at least $\mathcal{C}^{2-}$ across each cube face and along each cube edge.

The method of constructing the reference metric, $\tilde{g}_{ij}$, on multi-cube structures depends on the details of how each cubic region is connected to each of its neighbors: across each cube face, and along each cube edge. However this method does not depend on the global topological properties of the manifold, such as its orientability. This method can therefore be used to construct reference metrics on any non-orientable three-manifold, and has been used successfully to construct $\mathcal{C}^1$ metrics, $\tilde{g}_{ij}$, on each of the non-orientable manifolds included in this study: $P^2 \times S^1$, $P^2 \# P^2 \times S^1$, $P^2 \# T^2 \times S^1$, and $S^2 \tilde{\times} S^1$. The resulting positive-definite metrics $\tilde{g}_{ij}$ on these manifolds are smooth within each cubic coordinate chart, and are continuous and differentiable in the appropriate senses across the interfaces between cubic regions. These reference metrics, $\tilde{g}_{ij}$, are then used to construct the Jacobians that define the differentiable structure that determines the global continuity and differentiability of vectors and tensors on these manifolds [3, 8].

III. SIMPLE INITIAL DATA

This section describes the methods used in this study to find solutions to the Einstein initial value constraint equations. The goal is to construct initial data that can be used to evolve simple homogeneous cosmological models on these non-orientable manifolds. The Einstein constraint equations limit the allowed initial data for the spatial metric g_{ij} and extrinsic curvature K_{ij} on a spacelike hypersurface. The simplest solutions to these equations are determined by specifying a conformal metric, $\tilde{g}_{ij}$, and a constant, K, that functions as the trace of the extrinsic curvature on this initial surface. The physical metric g_{ij} and extrinsic curvature K_{ij} are given by

$$g_{ij} = \phi^4 \tilde{g}_{ij}, \tag{1}$$

$$K_{ij} = \tfrac{1}{3} \phi^4 \tilde{g}_{ij} K, \tag{2}$$

where ϕ is a conformal factor. This conformal factor is determined by solving the Einstein constraint equations, which for this simple case reduce to a second-order elliptic partial differential equation for ϕ.

This study follows the methods described in Ref. [4] for solving the Einstein constraint equations numerically on manifolds with non-trivial topologies. The conformal metrics $\tilde{g}_{ij}$ used in this study are the reference metrics constructed in Sec. II for each manifold. This study also assumes the average matter content in these solutions is negligible compared to the cosmological constant Λ. With these assumptions the Einstein constraint equation reduces to

$$\tilde{\nabla}^i \tilde{\nabla}_i \phi = \tfrac{1}{8} \phi \tilde{R} + \tfrac{1}{12} \phi^5 (K^2 - 3\Lambda), \tag{3}$$

where $\tilde{\nabla}_i$ and $\tilde{R}$ are the covariant derivative and Ricci scalar curvature respectively associated with the conformal metric $\tilde{g}_{ij}$.

The integral of the left side of Eq. (3) vanishes on any compact manifold. Therefore the constants K and Λ must be chosen in a way that makes it possible for the integral of the right side of this equation to vanish as well. Convenient choices for these constants would produce solutions to Eq. (3) with $\phi \approx 1$. Such choices can be identified by setting $\phi = 1$ in the expression on the right side of Eq. (3) and integrating over the manifold. Setting this integral to zero results in the values,

$$K^2 - 3\Lambda = -\tfrac{3}{2} \langle \tilde{R} \rangle, \tag{4}$$

where $\langle \tilde{R} \rangle$ is the average value of the conformal scalar curvature $\tilde{R}$,

$$\langle \tilde{R} \rangle = \frac{\int \sqrt{\tilde{g}}\, \tilde{R}\, d^3x}{\int \sqrt{\tilde{g}}\, d^3x}, \tag{5}$$

where $\tilde{g}$ represents the determinant of the conformal metric $\tilde{g}_{ij}$. This choice transforms Eq. (3) into the form

$$\tilde{\nabla}^i \tilde{\nabla}_i \phi = \tfrac{1}{8} \phi \left(\tilde{R} - \phi^4 \langle \tilde{R} \rangle \right). \tag{6}$$

This equation has the exact solution $\phi = 1$ in the constant scalar curvature case $\tilde{R} = \langle \tilde{R} \rangle$, and admits solutions on all the manifolds studied here. The integral of the right side of Eq. (3) must vanish for any solution ϕ. If $\phi > 0$ and $\tilde{R} > 0$ this integral can vanish only if $K^2 - 3\Lambda < 0$. Thus no $\phi > 0$ solution can exist to Eq. (3) when $\tilde{R} > 0$ unless the cosmological constant satisfies the inequality, $\Lambda > \frac{1}{3} K^2 \geq 0$.

The Ricci scalar curvature R determined from the physical metric g_{ij} is related to the Ricci scalar curvature $\tilde{R}$ associated with the conformal metric $\tilde{g}_{ij}$ by the expression

$$R = \phi^{-4} \tilde{R} - 8 \phi^{-5} \tilde{\nabla}^i \tilde{\nabla}_i \phi. \tag{7}$$

Solutions to the Einstein constraint Eq. (6) therefore have physical Ricci scalar curvatures given by

$$R = \langle \tilde{R} \rangle. \tag{8}$$

These simple solutions to the Einstein constraint equations therefore have the property that the physical scalar

curvature R is constant, $R = \langle \tilde{R} \rangle$. Thus the conformal factor ϕ is the solution to the Yamabe problem [9] that transforms $\tilde{g}_{ij}$ into the constant scalar curvature metric g_{ij}.

For this study the differential Eq. (6) has been solved numerically using the pseudo-spectral methods implemented in the SpEC numerical relativity code (developed initially by the Caltech and Cornell numerical relativity groups) as described in some detail in Refs. [4, 10]. These methods solve the non-linear Eq. (6) by minimizing the discrete version of the residual $\mathcal{E}$ defined by

$$\mathcal{E} = \tilde{\nabla}^i \tilde{\nabla}_i \phi - \tfrac{1}{8} \phi \left(\tilde{R} - \phi^4 \langle \tilde{R} \rangle \right). \tag{9}$$

Table I lists $\langle \tilde{R} \rangle$ defined in Eq. (5) and the physical volumes $\mathcal{V}$ defined by

$$\mathcal{V} = \int \sqrt{g}\, d^3x, \tag{10}$$

(where g is the determinant of the physical metric) for the geometries constructed for each of the manifolds included in this study. These volumes $\mathcal{V}$ measure the physical "sizes" of the manifolds in the length-scale units of our code, and can therefore be used to calibrate the sizes of the curvatures of the geometries.

TABLE I: Compact non-orientable manifolds included in this study. Also listed are the average scalar curvature $\langle \tilde{R} \rangle$ defined in Eq. (5), the physical volumes $\mathcal{V}$ defined in Eq. (10), and the cosmological constants Λ determined by Eq. (4) for the geometries with $K = -1$ constructed on each manifold.

Manifold	$\langle \tilde{R} \rangle$	$\mathcal{V}$	Λ
$P^2 \# P^2 \times S^1$	3.7×10^{-14}	4.000	0.3333
$P^2 \times S^1$	1.932	5.620	1.2992
$S^2 \tilde{\times} S^1$	2.693	9.349	1.6797
$P^2 \# T^2 \times S^1$	-3.866	4.113	-1.5998

The accuracy of the resulting numerical solutions can be evaluated by measuring how well they satisfy the constraints. The Hamiltonian constraint, $\mathcal{H}$, for the initial value problem considered here is given by the expression

$$\mathcal{H} = R + \tfrac{2}{3} \left(K^2 - 3\Lambda \right) = R - \langle \tilde{R} \rangle, \tag{11}$$

(see Ref. [4]). Consequently the Hamiltonian constraint norm $|| \mathcal{H} ||$ defined by,

$$|| \mathcal{H} ||^2 = \mathcal{V}^{-1} \int \left(R - \langle \tilde{R} \rangle \right)^2 \sqrt{g}\, d^3x, \tag{12}$$

is a useful tool for measuring the accuracy of the numerical solutions. Figure 3 illustrates the values of $|| \mathcal{H} ||$ as a function of the spatial resolution $N_{\rm grid}$ (the number of grid points in each direction of each multi-cube region) for each of the manifolds studied here. These numerical solutions are very time consuming for the higher resolution cases, and it is possible that the final results reported here could have been improved somewhat with more computer time or perhaps by setting somewhat different parameters in the PETSc solvers [11] used by the SpEC code. The results illustrated in Fig. 3 show that the numerical methods used in this study produce reasonably accurate, numerically convergent solutions to the Einstein initial value equations.

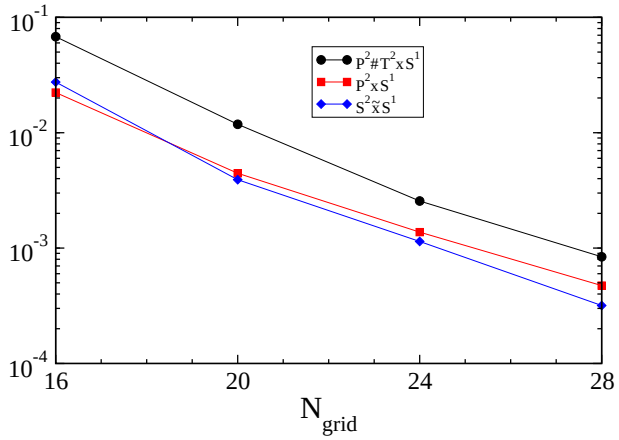

FIG. 3: This figure illustrates the norm of the Hamiltonian constraint, $|| \mathcal{H} ||$ defined in Eq. (12), as functions of the numerical resolution $N_{\rm grid}$ for the non-orientable manifolds $P^2 \# T^2 \times S^1$, $P^2 \times S^1$, and $S^2 \tilde{\times} S^1$. The values of $|| \mathcal{H} ||$ for the manifold $P^2 \# P^2 \times S^1$ are smaller than 6×10^{-10} for all values of $N_{\rm grid}$, and appears to be limited by double precision roundoff errors.

The Hamiltonian constraint norm, $|| \mathcal{H} ||$, is a measure of the homogeneity of the spatial Ricci scalar curvature R for these solutions. Therefore these initial data have good homogeneity in their scalar Ricci curvatures, R, as well as exact homogeneity in their extrinsic curvature traces, K. The homogeneity of these quantities are a necessary, but not sufficient, condition to ensure that the spacetimes evolved from these initial data remain homogeneous. In a homogeneous spacetime the initial data for the entire spatial Ricci tensor, R_{ij}, must also be homogeneous, not just its trace, R.

The homogeneity of the full spatial Ricci tensor can be explored further using the curvature scalar $\mathcal{R}$ defined by

$$\mathcal{R}^2 = 3 R_{ij} R^{ij}. \tag{13}$$

Its spatial average $\langle \mathcal{R} \rangle$ and spatial variations $\Delta \mathcal{R}$ are defined by

$$\langle \mathcal{R} \rangle = \frac{1}{\mathcal{V}} \int \sqrt{g}\, \mathcal{R}\, d^3x, \tag{14}$$

$$\Delta \mathcal{R} = \mathcal{R} - \langle \mathcal{R} \rangle. \tag{15}$$

An L_2 norm of these variations, $|| \Delta \mathcal{R} ||$ is defined by,

$$|| \Delta \mathcal{R} ||^2 = \frac{1}{\mathcal{V}} \int \sqrt{g}\, (\Delta \mathcal{R})^2\, d^3x, \tag{16}$$

is a useful measure of the homogeneity of $\mathcal{R}$. Table II compares the spatial variations in the Ricci scalar curvature, $||\,\mathcal{H}\,||$, the average values of the curvature scalar $\langle\mathcal{R}\,\rangle$, and the norm of the variations of the curvature scalar $||\,\Delta\mathcal{R}\,||$ in the initial data computed for each of the manifolds included in this study. These results show that while the full Ricci tensor in the initial data for the $P^2\#\,P^2\times S^1$ manifold is homogeneous, this is not the case for the other manifolds included in this study.

TABLE II: This table lists the average spatial variations in the scalar curvature $||\,\mathcal{H}\,||$ defined in Eq. (12), the average curvature scalar $\langle\mathcal{R}\,\rangle$ defined in Eq. (14), and the average spatial variations in the curvature scalar $||\,\Delta\mathcal{R}\,||$ defined in Eq. (16) for the $N_{\rm grid} = 28$ initial data on the manifolds included in this study.

Manifold	$\|\|\,\mathcal{H}\,\|\|$	$\langle\mathcal{R}\,\rangle$	$\|\|\,\Delta\mathcal{R}\,\|\|$
$P^2\#\,P^2\times S^1$	6.5×10^{-11}	5.9×10^{-11}	5.7×10^{-11}
$P^2\times S^1$	4.7×10^{-4}	4.40	3.63
$S^2\tilde{\times}S^1$	3.1×10^{-4}	5.25	2.82
$P^2\#\,T^2\times S^1$	8.5×10^{-4}	9.37	3.74

The reason the spatial Ricci tensor R_{ij} fails to be homogeneous, even for the physical metrics constructed by solving the Yamabe problem, can be traced to the properties of the conformal metric $\tilde{g}_{ij}$. The conformal metrics used for this study were the reference metrics constructed to define the differentiable structures on the multi-cube representations of the manifolds. These reference metrics were constructed from the basic structure of the multi-cube representation. They were designed to be C^{2-} across all the cube interfaces, but they were not designed to control the spatial dependence of the curvature within each cube. The conformal transformation used to solve the Yamabe problem forced homogeneity on the trace of the spatial Ricci tensor, but did not ensure the full Ricci tensor was homogeneous in most cases. Figure 4 illustrates the initial values of the curvature scalar variation, $\Delta\mathcal{R}$, for the $P^2\#\,T^2\times S^1$ manifold. The imprint of the multi-cube structure on the conformal metric $\tilde{g}_{ij}$ is clearly visible in this figure. The failure of the method used in this study to construct simple homogeneous initial data prevents us from constructing homogeneous cosmological models on most manifolds.

The curvature scalar $\mathcal{R}$ can also be used to detect anisotropy in these geometries. It's value is the same as the standard Ricci scalar curvature, $(\mathcal{R})^2 = R^2$, if the space is isotropic and all the eigenvalues of the Ricci tensor are the same. A rough measure of the isotropy of these spaces can therefore be obtained by comparing the average values of the Ricci scalar curvatures $\langle\tilde{R}\,\rangle$ from Table I with the average values of the curvature scalar $\langle\mathcal{R}\,\rangle$ from Table II. These results show that the initial data on the $P^2\#\,P^2\times S^1$ manifold is isotropic as well as homogeneous, but this is not the case for the other manifolds. The $\mathcal{R}^2$ curvature scalar is proportional to the sum of the squares of the eigenvalues of the Ricci tensor. In the $P^2\#\,P^2\times S^1$ manifold $\langle\mathcal{R}\rangle = 0$ to roundoff error accuracy, therefore the geometry on this manifold is flat.

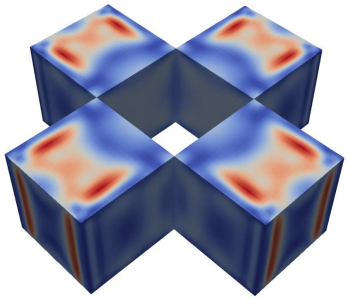

FIG. 4: This figure illustrates the inhomogeneity of the variations in the curvature scalar $\Delta\mathcal{R}$ defined in Eq. (15) for the initial data on the $P^2\#\,T^2\times S^1$ manifold.

IV. SIMPLE NON-ORIENTABLE COSMOLOGICAL MODELS

This section describes the methods used to construct simple non-orientable cosmological models by solving the Einstein evolution equations using the initial data prepared in Sec. III. The spatial metrics, g^0_{ij}, produced by those solutions to the Einstein constraint equations are used in two ways. First, they are used to construct the initial data for the spacetime metric ψ^0_{ab}:

$$ds^2 = \psi^0_{ab}dx^a dx^b = -dt^2 + g^0_{ij}dx^i dx^j, \qquad (17)$$

where the indices from the first part of the alphabet, e.g. a, b, c, ..., range over the four-dimensional spacetime coordinates, while the indices from the later parts of the alphabet, e.g. i, j, k, ..., range over the three-dimensional spatial coordinates on each t = constant hypersurface. Second, the metric ψ^0_{ab} is also used to define the time-independent spacetime reference metric, $\tilde{\psi}_{ab} \equiv \psi^0_{ab}$ that defines the differential structure in these four-dimensional manifolds.

The representation of the Einstein equation used to perform these evolutions is the covariant first-order symmetric-hyperbolic representation developed in Ref. [2]. The salient features of this representation are summarized in Appendix A. The dynamical fields in this representation are the spacetime metric, ψ_{ab}, its time derivative, $\Pi_{ab} = -t^c\tilde{\nabla}_c\psi_{ab}$, and its spatial derivatives $\Phi_{iab} = \tilde{\nabla}_i\psi_{ab}$, where t^c is the future directed timelike unit normal to the t = constant hypersurfaces. The covariant derivative, $\tilde{\nabla}_a$, used in these definitions is the one compatible with the reference metric: $\tilde{\nabla}_c\tilde{\psi}_{ab} = 0$. The values of the dynamical fields on the initial spacelike

hypersurface used to start these evolutions are given by,

$$\psi^0_{ab} = \tilde{\psi}_{ab}, \quad (18)$$
$$\Pi^0_{ta} = 0, \quad (19)$$
$$\Pi^0_{ij} = \tfrac{1}{3} K^0 g^0_{ij}, \quad (20)$$
$$\Phi^0_{iab} = 0, \quad (21)$$

where K^0 is the trace of the extrinsic curvature used to compute the initial data in Sec. III.

The first-order symmetric-hyperbolic representation of the Einstein system has a large number of constraints, which are described in some detail in Appendix A. The overall magnitude of these constraints is summarized by a quantity $\mathcal{C}_\psi$ defined in Eq. (A.12). The dimensionless norm $|| \mathcal{C}_\psi ||$ defined in Eq. (A.13) provides a useful measure of the fractional constraint violation errors in these cosmological models that is monitored during each numerical evolution.

An important goal of this study is to compare the simple non-orientable cosmological models constructed here with the standard orientable homogeneous and isotropic models. The spacetime metric for the standard cosmological models can be written in the form,

$$ds^2 = -d\eta^2 + a^2(\eta) L^2 \left[d\chi^2 + \Xi^2(\chi) \left(d\theta^2 + \sin^2\theta d\varphi^2 \right) \right], \quad (22)$$

where L is a characteristic length scale, $a(\eta)$ is a dimensionless scale factor, and $\Xi(\chi)$ is given by

$$\Xi(\chi) = \begin{cases} \sin\chi, & \text{for } k = +1, \\ \chi, & \text{for } k = 0, \\ \sinh\chi, & \text{for } k = -1, \end{cases} \quad (23)$$

for the orientable manifolds with positive, zero, and negative spatial curvatures respectively. The Einstein equations for these geometries are given by

$$\left(\frac{da}{d\eta} \right)^2 = -\frac{k}{L^2} + \frac{\Lambda}{3} a^2, \quad (24)$$
$$\frac{d^2 a}{d\eta^2} = \frac{\Lambda}{3} a, \quad (25)$$

in a spacetime where the cosmological constant Λ dominates over the matter content of the universe.

The properties of the non-orientable cosmological models resulting from the numerical evolutions performed for this study are most easily understood by expressing the resulting spacetime metric, ψ_{ab}, in the three-plus-one ADM form [12]:

$$ds^2 = \psi_{ab} dx^a dx^b = -N^2 dt^2 + g_{ij} (dx^i + N^i dt)(dx^j + N^j dt), \quad (26)$$

where N is the lapse, N^i the shift, and g_{ij} the spatial metric on each $t =$ constant hypersurface. It will also be helpful to define a scale factor $a(t)$ that measures how the determinant of the spatial metric, $g(t) = \det g_{ij}(t)$, evolves with time,

$$a(t)^6 = \frac{g(t)}{g(0)}. \quad (27)$$

The spatial average $\langle a(t) \rangle$, defined by

$$\langle a(t) \rangle^3 = \frac{\int \sqrt{g(t)}\, d^3x}{\int \sqrt{g(0)}\, d^3x} = \frac{\mathcal{V}(t)}{\mathcal{V}(0)}, \quad (28)$$

is a generalization of the scale factor used in the standard orientable homogeneous and isotropic cosmological models. Thus it will be interesting to compare the numerical evolution of $\langle a(t) \rangle$ in the non-orientable cosmological models constructed in this study with the analogous solutions for $a(\eta)$ from Eqs. (24) and (25). These comparisons are complicated by the fact that the gauge choices made to ensure stable numerical evolutions do not keep the shift $N(t)$ fixed at its initial value. Consequently the relationship between the numerical time coordinate, t, and the time coordinate, η, used on the standard cosmological models must be determined before comparisons between the cosmological models can be made.

It will also be useful to determine the extent to which the non-orientable cosmological solutions computed in this study are homogeneous. The spatial variations in $a(t)$, as defined in Eq. (27), can be measured with respect to its spatial average, $\langle a(t) \rangle$, by evaluating the norm $|| \Delta a ||$ defined by

$$|| \Delta a ||^2 = \frac{\int \left[a(t) - \langle a(t) \rangle \right]^2 \sqrt{g}\, d^3x}{\langle a(t) \rangle^2 \mathcal{V}(t)}, \quad (29)$$

Similarly the homogeneity of the lapse N can be evaluated:

$$|| \Delta N ||^2 = \frac{\int \left[N(t) - \langle N(t) \rangle \right]^2 \sqrt{g}\, d^3x}{\langle N(t) \rangle^2 \mathcal{V}(t)}, \quad (30)$$

where $\langle N(t) \rangle$ is defined by,

$$\langle N(t) \rangle = \frac{\int N(t) \sqrt{g}\, d^3x}{\mathcal{V}(t)}. \quad (31)$$

A. Simple Homogeneous Cosmological Model

The only homogeneous and isotropic initial data constructed in Sec. III were the data for the $P^2 \# P^2 \times S^1$ manifold. These initial data were evolved numerically until the spatial volume of the space grew to ten times its initial value. Figure 5 illustrates this volume increase by showing that the scale factor $a(t)$ increases from its initial value $a(0) = 1$ to the value $a(0.9) \approx 2.154$ at the end of the evolution. These evolutions were performed using multi-cube grids with resolutions $N_{\rm grid} = \{16, 20, 24, 28\}$ in each spatial direction.

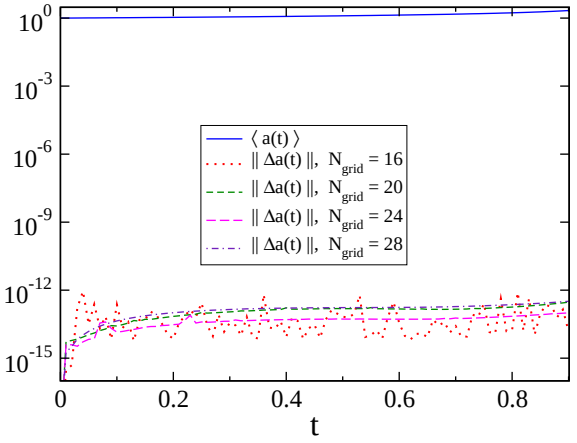

FIG. 5: This graph illustrates the average scale factor, $\langle a(t)\rangle$, and its spatial variations, $||\,\Delta a(t)\,||$, defined in Eqs. (28) and (29) for the evolutions on the $P^2\#\,P^2\times S^1$ manifold. The results of these evolutions for the spatial averages, $\langle a(t)\rangle$ using different resolutions are indistinguishable on the scale of this graph, so only the result from the highest resolution is shown.

Figure 6 illustrates the constraint norms $||\mathcal{C}_\psi||$ for these evolutions. These norms are all at about the 10^{-8} to 10^{-7} level and do not show significant (if any) convergence as $N_{\rm grid}$ increases. The lower limit on these norms is probably being set by the 10^{-7} time stepping tolerance used in these evolutions.

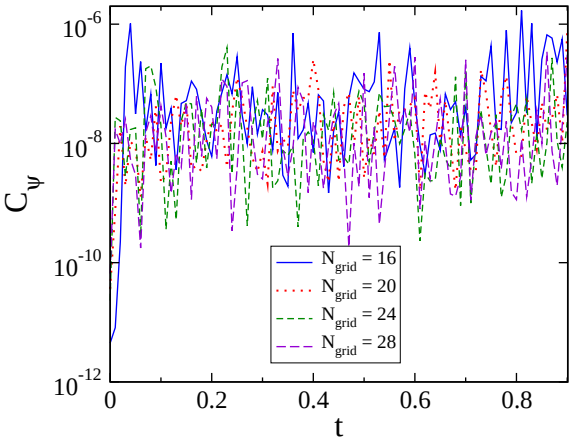

FIG. 6: This graph illustrates the constraint norm, $||\mathcal{C}_\psi||$, defined in Eq. (A.13) for the evolutions on the $P^2\#\,P^2\times S^1$ manifold.

Figures 5 and 7 illustrate the evolutions of the average scale factor $\langle a(t)\rangle$, the average lapse $\langle N(t)\rangle$ and their spatial variations $||\Delta a(t)||$ and $||\Delta N(t)||$ for the evolutions on the $P^2\#\,P^2\times S^1$ manifold. These graphs clearly show that both the scale factor $a(t)$ and the lapse $N(t)$ remain homogeneous at the double precision roundoff error level throughout these evolutions. Similar levels of homogeneity were also maintained (but not displayed to save space) by the other geometric scalars in these solutions, i.e. the

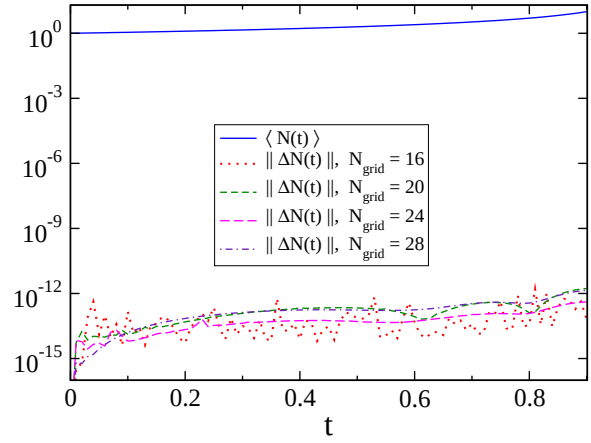

FIG. 7: This graph illustrates the average value of the lapse, $\langle N(t)\rangle$, and its spatial variations, $||\,\Delta N(t)\,||$, defined in Eqs. (31) and (30).

trace of the extrinsic curvature $K(t)$, the trace of the spatial Ricci curvature $R(t)$, and the curvature scalar $\mathcal{R}(t)$.

Figure 7 shows that the lapse $N(t)$ does not remain constant during the evolutions, increasing from its initial value $N(0) = 1$ to the value $N(0.9) = 10.0$ at the end. This implies that the time coordinate t used in the numerical evolutions is not the same as the time coordinate η used in the standard representations of the homogeneous cosmological models. Empirically we find that $\langle N\rangle \approx \langle a\rangle^3$ for the evolutions on the $P^2\#\,P^2\times S^1$ manifold, as demonstrated in Fig. 8 for the $N_{\rm grid} = 28$ evolution.

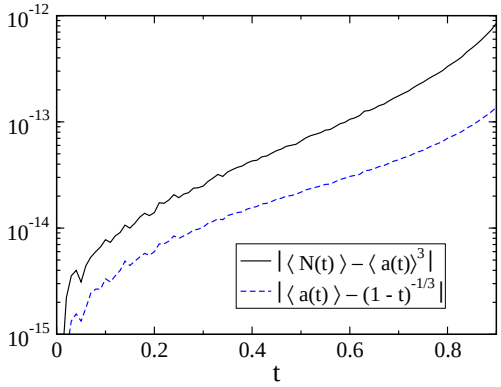

FIG. 8: The solid (black) curve in this graph demonstrates that $|\langle N\rangle - \langle a\rangle^3| < 9\times 10^{-13}$ for the $N_{\rm grid} = 28$ evolution on the $P^2\#\,P^2\times S^1$ manifold. Similarly the dashed (blue) curve in this graph demonstrates that $|\,\langle a(t)\rangle - (1-t)^{-1/3}\,| < 2\times 10^{-13}$ for this evolution.

The scale factor $a(\eta)$ is determined in the standard homogeneous cosmological models by Eq. (24). The constant k in that equation vanishes, $k = 0$, for the flat geometry on this $P^2\#\,P^2\times S^1$ manifold (see Table I),

thus Eq. (24) simplifies in this case to

$$\frac{da}{d\eta} = \sqrt{\frac{\Lambda}{3}}\, a. \tag{32}$$

Since $\langle N \rangle = \langle a \rangle^3$ for these evolutions (which are essentially homogeneous as shown in Figs. 5 and 7) it follows that $d\eta/dt = a^3$. Therefore Eq. (32) can be transformed into an equation for $a(t)$:

$$\frac{da}{dt} = \sqrt{\frac{\Lambda}{3}}\, a^4. \tag{33}$$

It is straightforward to integrate this equation analytically, with the result

$$a(t) = \left(1 - 3\sqrt{\frac{\Lambda}{3}}\, t\right)^{-1/3}. \tag{34}$$

The value of the cosmological constant Λ used for these evolutions is $\Lambda = 1/3$, see Table I. Therefore the analytic expression for $a(t)$ from Eq. (34) reduces to

$$a(t) = (1 - t)^{-1/3}. \tag{35}$$

Figure 8 shows that the numerical $\langle a(t) \rangle$ for these evolutions agrees with this analytical expression to within 2×10^{-13} for the $N_{\rm grid} = 28$ evolution.

B. Simple Inhomogeneous Cosmological Models

The initial data constructed in Sec. III on the $P^2 \times S^1$, $S^2 \tilde{\times} S^1$, and $P^2 \# T^2 \times S^1$ manifolds are significantly inhomogeneous, so the cosmological models evolved from them are not at all similar to the structure of our universe. These inhomogeneous models do, however, provide useful tests of the numerical methods that have been developed to solve Einstein's equation numerically on manifolds with arbitrary spatial topologies. Those methods had not previously been tested on significantly non-linear evolutions like the inhomogeneous cosmological models constructed here.

The initial data on the $P^2 \times S^1$ and $S^2 \tilde{\times} S^1$ manifolds were evolved in these tests until their spatial volumes increased by a factor of ten. The spatial volumes in the evolutions on the $P^2 \# T^2 \times S^1$ manifold increase initially, but then reach a maxima when their volumes are about 1.28 times their initial values. The volumes in the $P^2 \# T^2 \times S^1$ evolutions then contract and their evolutions were continued until their volumes returned to their initial values.

Perhaps the most interesting features of these inhomogeneous evolutions are the constraint norms $|| \mathcal{C}_\psi ||$. The evolution of these norms are shown in Fig. 9 for the $S^2 \tilde{\times} S^1$ manifold. The results for the $S^2 \tilde{\times} S^1$ and $P^2 \# T^2 \times S^1$ manifolds are qualitatively similar, and therefore will not be displayed to conserve space. The most important feature of these constraint norm graphs is the fact that they show excellent numerical convergence. These graphs show that value of $|| \mathcal{C}_\psi ||$ is reduced by a factor of about 0.8 as the spatial resolution $N_{\rm grid}$ is increased by four in each successive higher resolution evolution. This is the key indicator of exponential convergence, and shows that the numerical methods used in this study are producing exponentially convergent solutions to the Einstein evolution equations.

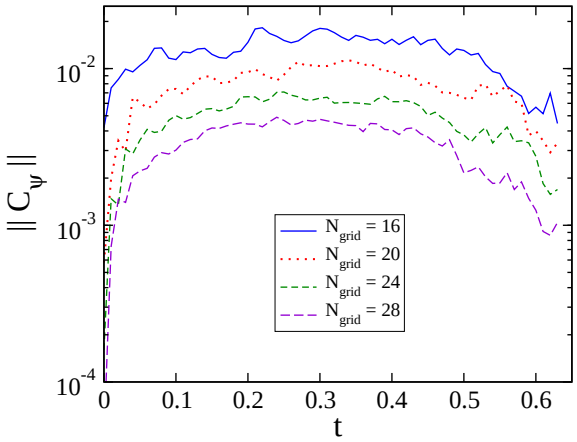

FIG. 9: This graph illustrates the dimensionless constraint norm, $|| \mathcal{C}_\psi ||$, defined in Eq. (A.13) for the evolutions on the $S^2 \tilde{\times} S^1$ manifold.

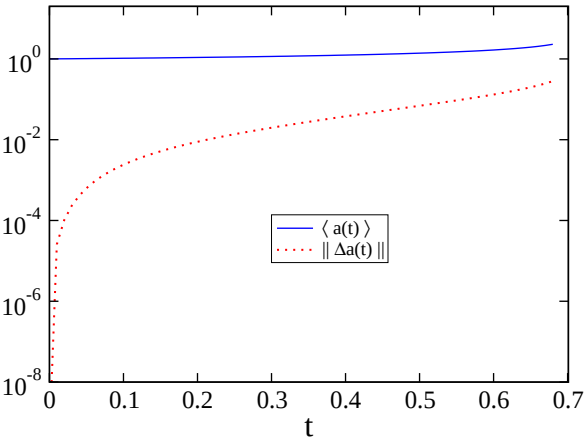

FIG. 10: This graph illustrates the average scale factor, $\langle a(t) \rangle$, and its spatial variations, $|| \Delta a(t) ||$, defined in Eqs. (28) and (29) for the evolutions on the $P^2 \times S^1$ manifold.

Figure 10 illustrates the average scale factor $\langle a(t) \rangle$ and the norm of its spatial variations $|| \Delta a(t) ||$ defined in Eqs. (28) and (29) for evolutions on the $P^2 \times S^1$ manifold. The results for the evolutions on the $S^2 \tilde{\times} S^1$ and $P^2 \# T^2 \times S^1$ manifolds are qualitatively similar. The results of these evolutions using different resolutions are indistinguishable on the scale of this graph, so only the results for the $N_{\rm grid} = 28$ case are shown. The most interesting feature of this figure is the fact that the spatial variation in the scale factor $|| \Delta a(t) ||$ increases from zero

in the initial data to about 0.2814 at the end of the evolution. This illustrates the significant inhomogeneity of these models.

Figure 11 illustrates the average value of the lapse $\langle N(t)\rangle$ and the norm of its spatial variations $||\,\Delta N(t)\,||$ defined in Eqs. (30) and (31) for evolutions on the $P^2\#\,T^2\times S^1$ manifold. The results for the evolutions on the $P^2\times S^1$ and $S^2\tilde{\times}S^1$ manifolds are qualitatively similar. The results of these evolutions using different resolutions are indistinguishable on the scale of this graph, so only the results for the $N_{\rm grid}=28$ case are shown. The most interesting feature of this figure is the fact that the spatial variation in the lapse $||\,\Delta N(t)\,||$ increases from zero in the initial data to about 0.04568 at the end of the evolution.

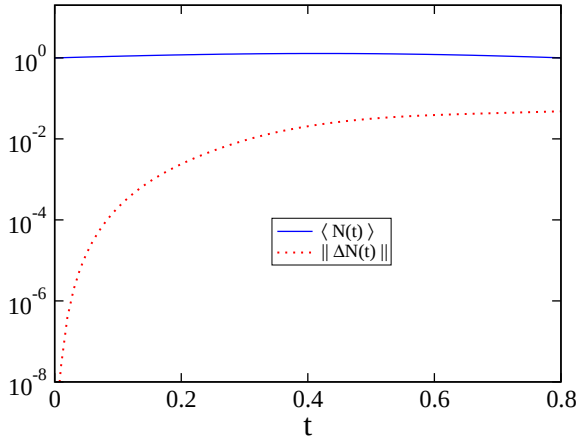

FIG. 11: This graph illustrates the average value of the lapse, $\langle N(t)\rangle$, and its spatial variations, $||\,\Delta N(t)\,||$, defined in Eqs. (30) and (31) for the evolutions on the $P^2\#T^2\times S^1$ manifold.

V. DISCUSSION

This study focused on applying and evaluating the numerical methods developed in recent years to solve Einstein's equation on manifolds with non-trivial topologies [1–4] by applying them to a study of simple cosmological models on manifolds with non-orientable spatial slices. Solutions to Einstein's equation were constructed on manifolds with spatial slices having the four non-orientable topologies: : $P^2\times S^1$, $P^2\#P^2\times S^1$, $P^2\#T^2\times S^1$, and $S^2\tilde{\times}S^1$. The Einstein constraint equations were solved numerically on these manifolds to produce initial data with homogeneous spatial Ricci scalar curvatures and constant extrinsic curvature traces. These initial data were then evolved numerically long enough to allow the spatial volumes of the manifolds to increase by a factor of ten. These numerical solutions were shown to be exponentially convergent on the manifolds $P^2\times S^1$, $P^2\#T^2\times S^1$, and $S^2\tilde{\times}S^1$. The extremely small constraint violations in the solutions on the $P^2\#P^2\times S^1$ manifold appear to be limited by double precision round-off errors for the elliptic initial data solves, and time-stepping errors for the hyperbolic evolutions. The numerical solutions on the manifold with spatial topology $P^2\#P^2\times S^1$ were shown to produce homogeneous cosmological solutions that agree with high precision locally to the corresponding Friedman cosmological model on an orientable manifold. The numerical solutions on the manifolds $P^2\times S^1$, $P^2\#T^2\times S^1$, and $S^2\tilde{\times}S^1$ were all shown to have significant inhomogeneities in their initial data, and these inhomogeneities were shown to grow as those initial data were evolved. While these inhomogeneous solutions do not make good cosmological models of our universe, they do serve as good tests of our numerical methods and their implementation in the `SpEC` code.

This study also reveals serious limitations in the method used to construct homogeneous initial data for cosmological models on manifolds with non-trivial topologies. In general, the reference metrics constructed by the method described in Ref. [3, 8] are not well suited to serve as the conformal metrics used to solve the initial data problem. These reference metrics have very inhomogeneous geometries that can not be made homogeneous by a simple conformal transformation. Better methods must be developed for constructing suitable conformal metrics on these manifolds. At this point perhaps the most promising method would be to smooth the current reference metrics by evolving them using Ricci flow [13]. We intend to explore this possibility in a future study.

Appendix A: Covariant First-Order Symmetric-Hyperbolic Einstein System

This study uses a covariant representation of the Einstein equations that enforces generalized harmonic gauge conditions [2]. The covariance of this representation is essential for the study of solutions on manifolds with multiple multi-cube coordinate patches, such as the non-orientable manifolds studied here. All the dynamical fields in this representation are tensors, so they can be transformed in a straightforward way across the interfaces between coordinate patches. The dynamical fields, u^α, for the first-order symmetric-hyperbolic representation of the Einstein equations used in this study are the collection of tensor fields,

$$u^\alpha=\{\psi_{ab},\Pi_{ab},\Phi_{iab}\}\,, \tag{A.1}$$

were ψ_{ab} is the spacetime metric, and the tensors Π_{ab} and Φ_{iab} represent its first derivatives,

$$\Pi_{ab} = -t^c\tilde{\nabla}_c\psi_{ab}, \tag{A.2}$$
$$\Phi_{iab} = \tilde{\nabla}_i\psi_{ab}. \tag{A.3}$$

The covariant derivative $\tilde{\nabla}_c$ used in these expressions is the one compatible with the reference metric $\tilde{\psi}_{ab}$: $\tilde{\nabla}_c\tilde{\psi}_{ab}=0$. This reference metric is also used to define the Jacobians used to transform tensor fields across

the boundary interfaces between multi-cube regions. The vector t^c represents the unit timelike normal to the spacelike hypersurfaces used to perform the evolutions. The lower range of Latin indices, e.g. a, b, c, ..., range over the four spacetime coordinates, while the higher range of indices, e.g. i, j, k, ..., range over the three spatial coordinates on each $t =$ constant hypersurface. The Greek indices, e.g. α, β, γ, range over the fifty components of the dynamical tensor fields u^α. The Einstein equations for these fields can be written in the first-order form

$$\partial_t u^\alpha + A^{k\alpha}{}_\beta(\mathbf{u})\tilde{\nabla}_k u^\beta = F^\alpha(\mathbf{u}, \tilde{\mathbf{\Gamma}}, \partial\tilde{\mathbf{\Gamma}}), \tag{A.4}$$

where the tensors $A^{k\alpha}{}_\beta(\mathbf{u})$ and $F^\alpha(\mathbf{u}, \tilde{\mathbf{\Gamma}}, \partial\tilde{\mathbf{\Gamma}})$ depend in complicated ways on the dynamical fields u^α, the reference connection $\tilde{\Gamma}^c{}_{ab}$ and its derivatives $\partial_d\tilde{\Gamma}^c{}_{ab}$. The detailed expressions for this representation of the covariant Einstein evolution system are given in Ref. [2].

The spacetime coordinates are determined in the generalized harmonic representations of Einstein's equation by imposing a condition on the difference between the connection $\Gamma^c{}_{ab}$ associated with the reference metric $\tilde{\psi}_{ab}$ and the physical connection $\Gamma^c{}_{ab}$ associated with the physical spacetime metric ψ_{ab}. In particular the difference between these connections is fixed by a gauge source function H_a:

$$H_a = -\psi_{ad}\,\psi^{bc}\left(\Gamma^d{}_{bc} - \tilde{\Gamma}^d{}_{bc}\right). \tag{A.5}$$

(Note that the difference between any two connections is a tensor.) In general H_a may be any function that depends on the physical metric ψ_{ab} (but not its derivatives) and the reference metric $\tilde{\psi}_{ab}$. The gauge condition used for the numerical evolutions performed in this study is the simple harmonic condition, $H_a = 0$.

The generalized harmonic evolution system contains a number of constraints. In particular the gauge condition, Eq. (A.5) is in effect a constraint

$$\mathcal{C}_a = H_a + \psi_{ad}\psi^{bc}\left(\Gamma^d{}_{bc} - \tilde{\Gamma}^d{}_{bc}\right). \tag{A.6}$$

on the dynamical fields. In addition, the equation that defines Φ_{iab}, Eq. (A.3), is also a constraint

$$\mathcal{C}_{iab} = \tilde{\nabla}_i\psi_{ab} - \Phi_{iab}. \tag{A.7}$$

These primary constraints, $\mathcal{C}_a$ and $\mathcal{C}_{iab}$, satisfy a second-order system of evolution equations as a consequence of the Einstein evolution system, Eq. (A.4). (See Ref. [2] for details.) This second-order constraint evolution system can be converted to a first-order symmetric hyperbolic system by introducing the secondary constraints,

$$\mathcal{F}_a = t^c\nabla_c\mathcal{C}_a, \tag{A.8}$$
$$\mathcal{C}_{ia} = \nabla_i\mathcal{C}_a, \tag{A.9}$$
$$\mathcal{C}_{ijab} = 2\tilde{\nabla}_{[i}\mathcal{C}_{j]ab}. \tag{A.10}$$

The symmetric-hyperbolic evolution equation for the collection of constraints,

$$\mathcal{C}^\alpha = \{\mathcal{C}_a, \mathcal{C}_{iab}, \mathcal{F}_a, \mathcal{C}_{ia}, \mathcal{C}_{ijab}\}, \tag{A.11}$$

ensures that solutions to the Einstein Eq. (A.4) that satisfy the constraints, $\mathcal{C}^\alpha$, on an initial surface will satisfy them throughout the evolution of those initial data. Numerical solutions to the equations will of course contain (hopefully small) violations of these constraints. This study monitors the size of these constraint violations by evaluating a norm constructed from the composite constraint, $\mathcal{C}_\psi$, defined by,

$$\mathcal{C}_\psi^2 = \delta^{ab}\left(\mathcal{C}_a\mathcal{C}_b + \mathcal{F}_a\mathcal{F}_b\right) + \tilde{g}^{ij}\delta^{ab}\delta^{cd}\left(\mathcal{C}_{iac}\mathcal{C}_{jbd} + \tfrac{1}{4}\tilde{g}^{kl}\mathcal{C}_{ikac}\mathcal{C}_{jlbd}\right). \tag{A.12}$$

This study evaluates a norm of $\mathcal{C}_\psi$, $||\,\mathcal{C}_\psi\,||$, defined by

$$||\,\mathcal{C}_\psi\,||^2 = \frac{\int \mathcal{C}_\psi^2\sqrt{g}\,d^3x}{\int \mathcal{N}_\psi^2\sqrt{g}\,d^3x}. \tag{A.13}$$

The quantity that appears in the denominator, $\mathcal{N}_\psi$, is defined by

$$\mathcal{N}_\psi^2 = \delta^{ab}\delta^{cd}\tilde{g}^{ij}\left(\partial_i\psi_{ac}\partial_j\psi_{bd} + \partial_i\Pi_{ac}\partial_j\Pi_{bd}\right) + \delta^{ab}\delta^{cd}\tilde{g}^{ij}\tilde{g}^{kl}\partial_i\Phi_{kac}\partial_j\Phi_{lbd}. \tag{A.14}$$

It has been included in the definition of $||\,\mathcal{C}_\psi\,||$ to provide a dimensionless measure of the fractional errors due to constraint violations in the numerical solutions to the Einstein evolution system.

Acknowledgments

We thank Michael Holst for providing the computational resources used to perform the numerical calculations reported in this study. We also thank James Nester for several helpful conversations about the geometry of non-orientable manifolds. L.L. was supported in part by grant No. 2407545 from the National Science Foundation to the University of California at San Diego, USA. F.Z. was supported by the National Key Research and Development Program of China grant 2023YFC2205801, and the National Natural Science Foundation of China grants 12433001 and 12021003.

[1] L. Lindblom, B. Szilágyi, J. Comput. Phys. **243**, 151 (2013)

[2] L. Lindblom, B. Szilágyi, N.W. Taylor, Phys. Rev. D **89**, 044044 (2014)

[3] L. Lindblom, N.W. Taylor, O. Rinne, J. Comput. Phys. **313**, 31 (2016)

[4] F. Zhang, L. Lindblom, Gen. Relativ. Gravit. **54**, 131 (2022)

[5] R. Geroch, Journal of Mathematical Physics **9**, 1739 (1968)

[6] R. Geroch, Journal of Mathematical Physics **11**, 343 (1970)

[7] B. Grinstein, R. Rohm, Commun. Math. Phys. **111**, 667 (1987)

[8] L. Lindblom, O. Rinne, N.W. Taylor, J. Comput. Phys. **410**, 110957 (2022)

[9] H. Yamabe, Osake J. Math. **12**, 21 (1960)

[10] H.P. Pfeiffer, L.E. Kidder, M.A. Scheel, S.A. Teukolsky, Comput. Phys. Commun. **152**, 253 (2003)

[11] S. Balay, S. Abhyankar, M.F. Adams, S. Benson, J. Brown, P. Brune, K. Buschelman, E. Constantinescu, L. Dalcin, A. Dener, V. Eijkhout, W.D. Gropp, V. Hapla, T. Isaac, P. Jolivet, D. Karpeev, D. Kaushik, M.G. Knepley, F. Kong, S. Kruger, D.A. May, L.C. McInnes, R.T. Mills, L. Mitchell, T. Munson, J.E. Roman, K. Rupp, P. Sanan, J. Sarich, B.F. Smith, S. Zampini, H. Zhang, H. Zhang, J. Zhang, PETSc/TAO users manual. Tech. Rep. ANL-21/39 - Revision 3.16, Argonne National Laboratory (2021)

[12] R. Arnowett, S. Deser, C.W. Misner, in *Gravitational: An Introduction to Current Research*, ed. by L. Witten (Wily, New York, 1962), pp. 227–265

[13] B. Chow, D. Knopf, *The Ricci Flow: An Introduction*, *Mathematical Surveys and Monographs*, vol. 110 (Amer. Math. Soc., 2004)